

See discussions, stats, and author profiles for this publication at: <https://www.researchgate.net/publication/225406093>

Computational Investigation of the Thermochemistry and Kinetics of Steam Methane Reforming Over a Multi-Faceted Nickel Catalyst

ARTICLE *in* TOPICS IN CATALYSIS · SEPTEMBER 2011

Impact Factor: 2.37 · DOI: 10.1007/s11244-011-9704-z

CITATIONS

18

READS

37

3 AUTHORS, INCLUDING:



D. Wayne Blaylock

Dow Chemical Company

10 PUBLICATIONS 131 CITATIONS

SEE PROFILE



Yi-An Zhu

East China University of Science and Techn...

32 PUBLICATIONS 341 CITATIONS

SEE PROFILE

Computational Investigation of the Thermochemistry and Kinetics of Steam Methane Reforming Over a Multi-Faceted Nickel Catalyst

D. Wayne Blaylock · Yi-An Zhu · William H. Green

Published online: 20 August 2011
© Springer Science+Business Media, LLC 2011

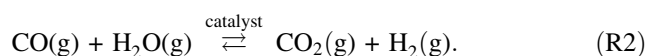
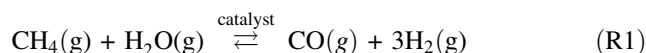
Abstract A microkinetic model of steam methane reforming over a multi-faceted nickel surface using plane-wave, periodic boundary condition density functional theory is presented. The multi-faceted model consists of a Ni(111) surface, a Ni(100) surface, and nickel step edge sites that are modeled as a Ni(211) surface. Flux and sensitivity analysis are combined to gain an increased understanding of the important reactions, intermediates, and surface facets in SMR. Statistical thermodynamics are applied to allow for the investigation of SMR under industrially-relevant conditions (e.g., temperatures in excess of 500 °C and pressures in excess of 1 bar). The most important surface reactions are found to occur at the under-coordinated step edge sites modeled using the Ni(211) surface as well as on the Ni(100) surface. The primary reforming pathway is predicted to be through $C^* + O^* \rightarrow CO^*$ at high temperatures; however, hydrogen-mediated reactions such as $C^* + OH^* \rightarrow COH^*$ and $CH^* + O^* \rightarrow CHO^*$ are predicted to become more important at low temperatures. The rate-limiting reactions

are predicted to be dissociative chemisorption of methane in addition to the aforementioned C–O addition reactions.

Keywords Computational thermal chemistry · Steam reforming of methane · Nickel catalysts · Computational heterogeneous catalysis

1 Introduction

The production of hydrogen has long been of interest due to its importance as a feedstock in the chemical industry, with applications such as petrochemical processing and the creation of ammonia for fertilizer production [1]. More recently, interest has also turned to consideration of hydrogen as a potential energy-carrier in future energy infrastructures. Currently, the primary means of hydrogen production is steam reforming of hydrocarbons, particularly steam methane reforming (SMR), which is responsible for 95% of the hydrogen production in the United States [2]. SMR is coupled with the water–gas shift (WGS) reaction to produce hydrogen via the process:



SMR is typically carried out at temperatures ranging from 600 to 900 °C and pressures of 10–30 bar. Because hydrogen is widely-produced from fossil fuels, it is not a carbon-free energy source. As a result, researchers have been engaged in the development of membrane reactors capable of the in situ separation of the $CO_2(g)$ and $H_2(g)$ products, allowing for subsequent sequestration of the carbon dioxide [3–5]. In addition to traditional

D. W. Blaylock · W. H. Green (✉)
Department of Chemical Engineering, Massachusetts Institute of Technology, 77 Massachusetts Ave, Cambridge, MA 02139, USA
e-mail: whgreen@mit.edu

Present Address:
D. W. Blaylock
Engineering and Process Science, Core R&D, The Dow Chemical Company, 1710 Building, Midland, MI 48674, USA

Y.-A. Zhu
State Key Laboratory of Chemical Engineering, East China University of Science and Technology (ECUST), 130 Meilong Road, Shanghai 200237, China

hydrogen production, the kinetics of the SMR and WGS reactions are an active area of research with regard to internal reforming in solid oxide fuel cells [6–8]. Historically, nickel is the preferred SMR catalyst because of its reasonably high activity and affordability relative to noble metal catalysts [9]. However, nickel is susceptible to deactivation via carbon formation, which can be exacerbated in membrane reformers, where hydrogen partial pressure is low, and solid oxide fuel cells, where high steam to methane ratios are generally avoided [7, 10, 11]. Concerns over deactivation via carbon formation motivate interest in new catalysts that inhibit carbon formation while retaining activity to the steam reforming reaction. To aid in the search for improved SMR catalysts, a detailed understanding of the important reactions and intermediates on the nickel surface is desired. Efforts have previously been made to gain a detailed understanding of the reactions occurring on the catalyst surface. For example, Wei and Iglesia [12] showed that the SMR rate is insensitive to hydrogen and water partial pressures at high temperatures, indicating that under those conditions methane chemisorption is rate-controlling. Xu and Froment [13] have proposed a multistep mechanism to describe SMR kinetics and Aparicio [14] and Chen, et al. [15] have applied experimentally-parameterized microkinetic models to provide greater mechanistic detail of SMR, including deactivation effects. Microkinetic modeling is an attractive technique for obtaining detailed information about surface reactions and intermediates because it applies elementary reactions with no assumption of rate-determining step [16].

In addition to experiment, computation has also been applied to the parameterization of microkinetic models. Chen et al. have recently employed the activation exponential potential (UBI-QEP) approach and transition state theory to the microkinetic modeling of SMR [17]. Furthermore, density functional theory (DFT) has become a popular computational tool for describing heterogeneous catalysis, including many recent applications to methane reforming [18–22]. Previously, we applied DFT to develop a detailed microkinetic model to describe SMR over Ni(111) at industrially-relevant conditions [23]. While the resulting model agrees well with several comparisons to single-crystal data, it significantly under-predicts observed reforming rates over commercial, multifaceted catalysts. In the previous work, we identified that a likely contributor to this disagreement was the lack of other facets of the nickel surface in the kinetic model, in particular under-coordinated step sites. While the reforming pathway through direct formation of CO* from C* and O* has been studied at the nickel step edge [18, 21], other potential pathways (Fig. 1) have remained largely unexplored on nickel surfaces other than the (111) facet. In the present study, we extend our multiple-pathway analysis of SMR over Ni(111)

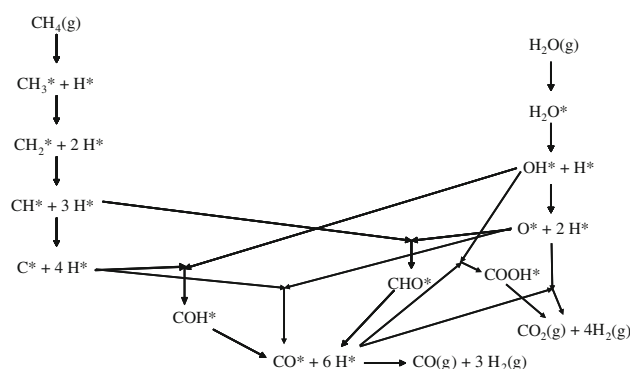


Fig. 1 Steam methane reforming mechanism investigated on Ni(111), Ni(211), and Ni(100)

to develop an ab initio microkinetic model of steam methane reforming over a multi-faceted nickel catalyst.

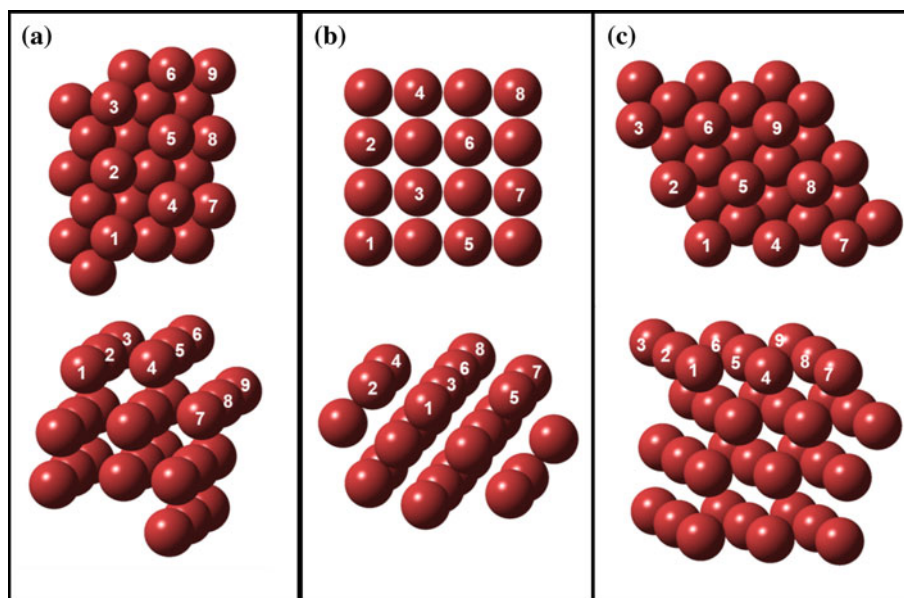
We include the effects of the Ni(111), Ni(100), and Ni(211) surface facets. The Ni(111) and Ni(100) surface facets are the most abundant facets of nickel and the Ni(211) surface is employed as a surrogate surface to model the effects of under-coordinated step edge sites. Density functional theory, statistical thermodynamics and transition state theory are used to compute the thermochemistry and kinetics of the mechanism shown in Fig. 1 on each of these surfaces. The thermochemical and kinetic values for each surface are combined in a mean-field, microkinetic model to simulate SMR at industrial reforming conditions over a multifaceted nickel catalyst. The microkinetic model is used to investigate the primary reforming pathways, including the relative activity of each surface facet to the reactions included in the mechanism. The microkinetic model provides insight into the rate-limiting reactions as well as the most dominant surface species on each surface facet. In addition, incorporation of the microkinetic model into a plug-flow reactor model allows for comparison of the model's results to experimentally-observed rates of methane conversion.

2 Computational Methods

2.1 Quantum Chemical Calculations

Plane wave, periodic boundary condition DFT calculations are performed in the Vienna Ab Initio Simulation Package (VASP) [24–26]. The calculations consider three model surfaces: the (111), (100), and (211) surface facets (see Fig. 2) of a FCC crystal of nickel atoms at the experimental lattice parameter (3.52 Å). For (111) surface calculations, a supercell consisting of a 3×3 unit cell of four layers of metal atoms with approximately 10 Å of vacuum spacing between periodic images of the metal slab is employed,

Fig. 2 Unit cells for the **a** 211, **b** 100, and **c** 111 surface facets of the Ni catalyst



with the top two layers of the metal slab being relaxed in all optimizations. The supercell used to model the (100) surface facet consists of a 2×2 unit cell, with three layers of metal atoms and approximately 10 Å of vacuum spacing separating periodic slab images. The top layer of metal atoms are relaxed for the (100) slab in all optimizations. Note that the “clock” reconstruction of the (100) surface is not considered in this study [27]. The (211) surface facet is modeled using a 3×1 unit cell of nine layers of metal atoms (e.g., the three atoms in a row of the top-most level of atoms each have a different z-coordinate, making nine layers for a unit cell that is three atoms deep per row), with periodic images of the metal slab being separated by approximately 12 Å of vacuum spacing. For the (211) slab, the top layer of metal atoms are relaxed in all optimizations. The application of a dipole correction to electrostatically decouple the periodic slabs is not employed after test cases for H^* , O^* , and CHO^* found its effect to be less than 1 kJ/mol in binding energy. A 15^3 Å^3 cube unit cell is used to study isolated gas phase atoms and molecules.

In our DFT calculations, we use the RPBE [28] functional and apply the first order Methfessel-Paxton method for electron smearing along with spin polarization. The RPBE functional has been shown to be more accurate than other functionals such as PW91 and PBE in calculating heats of adsorption on nickel for molecules relevant in this study [29]. Projector-augmented wave (PAW) potentials [30] are used to describe the effect of core electrons, while the valence states were expanded with an energy cutoff of 400 eV. The Brillouin zone is sampled by (3,3,1), (4,4,1), and (4,3,1) *k*-point Monkhorst–Pack grids for the (111), (100), and (211) surface facets, respectively. Convergence tests were conducted when choosing the selected values

energy cutoff, slab thickness, and *k*-point spacing and energies were found to be reasonably well converged for the stated values of these parameters. Specifically, adding a fifth layer to the (111) slab or a fourth layer of metal atoms to the (211) and (100) slabs was found to change binding energies by less than 0.03 eV on average. The energy cutoff was found to be converged within 0.03 eV relative to a cutoff of 500 eV for the binding energy of O^* on Ni(111). In addition, the *k*-point spacing was found to be converged within an average of 0.03 eV in binding energies relative to (5,5,1), (6,6,1), and (6,5,1) *k*-point spacings for the (111), (100), and (211) surfaces, respectively.

In geometry optimizations and first-order saddle point calculations for reaction transition states, all adsorbate atoms and the top layer of metal atoms are relaxed. First-order saddle point calculations for transition state geometries are carried out using the dimer method [31]. In some cases, initial guess geometries for the dimer calculations are obtained using the climbing-image nudged elastic band (CI-NEB) method [32]. Geometry optimizations are carried out until the change in energy between successive ionic relaxations is less than $1\text{E-}4$ eV. First-order saddle point searches are considered converged when all forces are less than $1\text{E-}3$ eV/Å.

Harmonic vibrational frequency analysis is performed on stable adsorbate and transition state geometries to obtain frequencies for calculation of kinetic parameters. In addition, frequencies for the transition states are used to confirm that the negative mode for each transition state corresponds to the desired reaction coordinate. The vibrational frequency calculations are performed using the dynamical matrix code [33] in VASP, with a tighter convergence parameter of $1\text{E-}6$ eV/Å on forces to ensure better-converged frequencies.

2.2 Species Thermochemistry

The enthalpy, entropy, and Gibbs free energy are computed for each species as a function of temperature. The partition functions used to calculate thermodynamic quantities are computed using expressions previously published in our investigation of SMR over single-crystal Ni(111) [23]. In the previous work, partition functions were applied to describe translation and rotation as either free or frustrated (e.g., two-dimensional gas with free translation vs. a tightly bound adsorbate with only frustrated translation). Of the adsorbates included in the current mechanism, only H_2O^* and CO_2^* were found to be weakly-bound, freely rotating and translating molecules in the previous work. In addition, the transition state for hydrogen adsorption was treated as freely translating. These same treatments are extended to these species and transition state in this work, with the partition functions being calculated as described in the previous work.

The experimentally-adjusted heats of adsorption procedure described in our previous work for SMR over single-crystal Ni(111) is applied to the calculated heats of adsorption for the (111) surface in the present study. The experimentally-adjusted heats of adsorption for the (211) and (100) surfaces are computed by adding the difference in DFT-computed binding energies for a species on the surface of interest and the species on the (111) surface to the experimentally-adjusted heat of adsorption for that species on the (111) surface.

2.3 Estimation of Fractional Coverage of Each Surface Facet

To obtain a theoretical prediction of equilibrium particle shape, the nickel nanoparticle is assumed to be a truncated octahedron with eight hexagonal (111) and six square (100) facets on its surface. The truncated octahedron shape has been shown to be a reasonable equilibrium model for nanoparticles with surface energies similar to those exhibited by nickel [34]. Consistent with previous computational methodology as well as experimental observation [35, 36], the atoms along the interfaces where (111) facets intersect with other (111) or (100) facets are assumed to be unstable and lost into solution, thus creating step edges. The thermochemistry and kinetics of the step edge atoms are modeled using the (211) surface facet.

The total number of step edge atoms is approximated as the sum of edge and vertex atoms on the truncated octahedron. The number of (111) atoms, (100) atoms, and step edge atoms are calculated using the appropriate equations reported by Li, et al., which are functions of n_{squ} and n_{hex} , the number of edge atoms along the (111)–(100) and (111)–(111) interfaces, respectively [34]. Note that an error exists

in Eq. 2.1 of Li, et al., where the factor of 4 should be placed outside the left bracket, not inside. The particle size is calculated from the average of the distances from the center of the particle to the center of a (111) facet and to the center of a (100) facet, assuming a nickel lattice parameter of 3.52 Å. The values used for the surface energy of Ni(100) and Ni(111) are 2.88 J/m² and 2.44 J/m², respectively [37].

2.4 Microkinetic Model

A mean-field, microkinetic model is constructed by combining the computed thermochemical and kinetic values for each surface facet with the surface facet fractional abundance data gained through particle shape analysis. The kinetic model is used to gain an understanding of reforming pathways, through flux analysis, and the relative degree of rate limitation of the reactions in the mechanism, through sensitivity analysis. For flux and sensitivity analyses, a continuous-stirred tank reactor (CSTR) formulation is employed. The reactions in the kinetic model can be categorized as either (1) the adsorption/desorption of a species onto/from a surface facet, (2) a surface reaction with all species on a single surface facet, and (3) the diffusion of an adsorbed surface species from one surface facet to another. The diffusion between surface facets is treated as a reaction in the model because it involves the disappearance of a surface species from/on a surface facet.

2.4.1 Rate Expressions

The molar rate of change for a surface species i on surface facet f_s is expressed as a sum of the rate of change due to reaction (Eq. 1) and the rate of change due to inter-facet diffusion (Eq. 2).

$$r_{i,f_s,\text{RXN}} = \sum_{j \text{ on } f_s} v_{j,i} \left[k_{j,f_s} \prod_{l=1}^{S_R} C_{l,f_s}^{-v_{j,l}} - k_{-j,f_s} \prod_{l=1}^{S_P} C_{l,f_s}^{v_{j,l}} \right], \quad (1)$$

where $v_{j,i}$ is the stoichiometric coefficient of component i in reaction j , k is the rate coefficient for the forward (j) and reverse ($-j$) reactions on surface facet f_s , C is the concentration (in fractional coverage for vacant sites, mol/m² for adsorbates, and mol/m³ for gas phase species) of component l (on surface facet f_s when the subscript l denotes a surface species). The molar rate of change for species i due to diffusion to/from surface facet f_s from/to another facet of the catalyst, f_t , is described as.

$$\begin{aligned} r_{i,f_s,\text{Diff},f_{s,t}} &= -\left(\frac{\alpha_{f_t}}{\alpha_{f_s}}\right) r_{i,f_t,\text{Diff},f_{s,t}} \\ &= -k_{i,f_{s,t}} C_{i,f_s} C_{*,f_t} + k_{i,-f_{s,t}} C_{i,f_t} C_{*,f_s}, \end{aligned} \quad (2)$$

where α is the surface area of the subscripted facet, subscripts $f_{s,t}$ and $-f_{s,t}$ indicate forward and reverse

diffusion from surface facet f_s to facet f_t , and the subscript * represents a vacant site (recall that the concentration of vacant sites is expressed in terms of fractional coverage). Note that Eq. 2 describes diffusion to/from facet f_s from/to one other facet and must be summed over all facets $f_{s,t} \neq s$ to capture all inter-facet diffusion, resulting in a total rate of change for species i on surface facet f_s of.

$$\frac{dC_{i,f_s}}{dt} = r_{i,f_s, \text{RXN}} + \sum_{i \neq s} r_{i,f_s, \text{Diff}, f_{s,t}} \quad (3)$$

For flowing gaseous species, the molar rate of change for a species is expressed as a sum of the rate of change due to adsorption/desorption and rate of change due to flow into/out of the reactor. The total molar rate of change for gaseous species i is expressed as

$$\frac{dC_i}{dt} = \sum_s \left(\frac{\alpha_{f_s}}{V} \right) r_{i, \text{Ads}, f_s} + \frac{C_{i, \text{in}}}{\tau_{\text{res}, o}} - \frac{C_i}{\tau_{\text{res}}} \quad (4)$$

where V is the volume of the reactor, r_{i, Ads, f_s} is the net rate of change of gas phase species i due to adsorption/desorption onto/from surface facet f_s , $\tau_{\text{res}, o}$ is the user-specified zero-conversion residence time of the CSTR, and $C_{i, \text{in}}$ is the inlet concentration of gaseous species i . Note that the value $r_{i, \text{Ads}/\text{Des}, f_s}$ is calculated using Eq. 1, where $r_{i, \text{Ads}/\text{Des}, f_s}$ is equal to $-r_{i, f_s, \text{RXN}}$ and i_{f_s} is the product of the adsorption of gas phase species i onto surface facet f_s .

The zero-conversion residence time is equal to the actual reactor residence time for systems with no net change in moles upon reaction. For reactions where there is a net change in number of moles upon reaction, the two residence times are approximately equal at low conversions; however, to allow for the investigation of larger conversions, the actual reactor residence time, τ_{res} , is calculated as:

$$\begin{aligned} \tau_{\text{res}} &= \frac{n_T}{F_T} = \left(\frac{PV}{RT} \right) \left(\frac{1}{F_T} \right) \\ &= \left(\frac{PV}{RT} \right) \left(\frac{1}{F_{T, o}} \right) \left(\frac{1}{1 + \Delta F/F_{T, o}} \right) \\ &= \left(\frac{\tau_{\text{res}, o}}{1 + \Delta F/F_{T, o}} \right), \end{aligned} \quad (5)$$

where n_T is the total number of gas phase moles in the CSTR, F_T is the total molar flow rate out of the reactor, ΔF is the change in molar flow rate from the initial feed to the outlet of the CSTR, and the subscript o represents an initial, or zero-conversion, quantity. With specific regard to the overall reactions studied in this work (the steam methane reforming reaction paired with water gas shift), the change in number of moles upon reaction at a specific methane conversion is expressed as a function of initial and final methane mole fractions, $y_{\text{CH}_4, \text{feed}}$ and y_{CH_4} , through

$$\frac{\Delta F}{F_{T, o}} = \left(\frac{y_{\text{CH}_4, \text{feed}} - y_{\text{CH}_4}}{0.5 + y_{\text{CH}_4}} \right) \quad (6)$$

The complete set of time-dependent CSTR equations (one for each gas phase or surface species) must then be solved using a differential equation solver, time-stepping to steady state for a specified zero-conversion residence time. In this work, ODE15s in MATLAB is employed.

The time-dependent CSTR equations are also extended to solve for the axial concentration profile of an ideal plug-flow reactor (PFR). Applying the method of lines to the one-dimensional, time-independent design equation for a PFR and assuming negligible axial dispersion, one arrives at an approximation of the PFR as a series of CSTRs where the number of CSTRs is defined by the number of discretizations performed in the axial direction. For the PFR, the residence time is no longer user-specified, but is instead defined by the reactor conditions and molar flow rate in the section of interest. Assuming isobaric and isothermal operation, the residence time for section r is expressed as.

$$\tau_{\text{PFR}_\text{res}, r} = \frac{n_{T, r}}{F_{T, r}} = \left(\frac{P}{RT} \right) \left(\frac{\varepsilon}{\rho_{\text{cat}}} \right) \left(\frac{m_{\text{cat}, r}}{F_{T, r}} \right), \quad (7)$$

where $n_{T, r}$ is the total number of gas phase moles in section r at pressure P and temperature T , $F_{T, r}$ is the total molar flow rate through the reactor section, ε is the void fraction of the packed catalyst bed, ρ_{cat} is the bulk density of catalyst in the bed (total mass of catalyst divided by volume of the bed), and $m_{\text{cat}, r}$ is the mass of catalyst in section r . Also, note that when the ratio (α_{f_s}/V) in Eq. 4 is expressed in the same variables as $\tau_{\text{PFR}_\text{res}, r}$ for the PFR formulation, it becomes

$$\left(\frac{\alpha_{f_s}}{V} \right)_{\text{CSTR}} = \left(\frac{\alpha_{f_s} \rho_{\text{cat}}}{\varepsilon} \right)_{\text{PFR}}, \quad (8)$$

where α is the total area of facet f_s per unit catalyst mass. The change in number of moles from PFR inlet to section r must be taken into consideration, using Eq. 6 to solve for the flow rate as a function of conversion, analogous to the CSTR formulation. To solve for the concentration profiles in the PFR, each of the N_{sections} CSTRs is integrated to steady state (in a manner identical to that for the single CSTR described above), in succession from $r = 1$ to $r = N_{\text{sections}}$, subject to the constraint that the sum of the catalyst mass per section over all sections is equal the total mass of catalyst in the PFR. After the first section is solved using the PFR feed conditions, the outlet species concentrations from section $r-1$ serve as the feed composition for section r . Thus, the re-expression of Eq. 4 for the PFR formulation takes the form.

$$\begin{aligned} \left(\frac{dC_i}{dt} \right)_r &= \sum_s \left[\left(\frac{\alpha_{f_s} \rho_{\text{cat}}}{\varepsilon} \right)_{\text{PFR}} r_{i, \text{Ads}, f_s} \right] \\ &+ \left(\frac{C_{i, r-1}}{\tau_{\text{PFR}_\text{res}, r, o}} - \frac{C_i}{\tau_{\text{PFR}_\text{res}, r}} \right), \end{aligned} \quad (9)$$

where, similar to Eq. 4, $\tau_{\text{PFR}_{\text{res},r,o}}$ is the zero-conversion residence time of reactor section r . This quantity is calculated analogously to the zero-conversion residence time in the CSTR formulation by dividing the volume of reactor section r by the inlet molar flow rate to the section (which in the PFR formulation is the outlet molar flow rate of section $r-1$).

2.4.2 Rate Coefficients

The expressions for the rate coefficients describing adsorption/desorption reactions and reactions between adsorbed species on a single surface facet are taken from our previous analysis of SMR on single-crystal Ni(111). In this work, we add an expression for the rate coefficient describing inter-facet diffusion of a species on a multi-faceted catalyst. The rate coefficient describing the disappearance of species A^* from surface facet f_s due to inter-facet diffusion to surface facet f_i is defined as

$$k_{\text{for}} = \left(\frac{k_B T}{h} \right) \left(\frac{q_{A^{**\dagger}}}{q_{A^*f_s} q_{*f_i}} \right) \exp \left(\frac{-E_o}{RT} \right) \left(\frac{M_{\text{Int}}}{M_{f_s}} \right), \quad (10)$$

where M_{Int} is the number of interfacial binding sites between the two surface facets, M_{f_s} is the number of binding sites on surface facet f_s , and the ratio M_{Int}/M_{f_s} represents the probability of a binding site on facet f_s bordering a binding site on facet f_i . The ratio is equivalent to the “inhomogeneity parameter,” $\omega_{1,2}$, applied by Cwiklik to the problem of mean-field modeling of diffusion on non-uniform surfaces [38]. Note that the rate coefficient in Eq. 10 is written for the rate expression describing the disappearance of species A^* from surface facet f_s . Had the rate coefficient been written for the rate expression describing the appearance of species A^* on surface facet f_i , the rate coefficient would have also included the correction (C_{Tf_i}/C_{Tf_s}) , where C_T represents the molar concentration of binding sites on the subscripted surface facet.

Consistent with the application of the mean-field model, there exists an assumption in Eq. 10 that intra-facet diffusion is sufficiently fast that there are no concentration gradients near the interface of neighboring facets. Thus, an adsorbate on surface facet f_s (e.g., $A^*_{f_s}$) located at the interface between facets f_s and f_i diffuses to the average vacant site fraction on facet f_i . Because diffusion in this system generally involves lower activation barriers than surface reactions, the diffusion in the mean-field model will often be considerably faster than surface reactions. Thus, obtaining accurate pre-exponential factors for diffusion is not as important as obtaining the pre-factors for adsorption and surface reactions. For inter-facet diffusion, all pre-factors are estimated to be $1 \times 10^{12} \text{ s}^{-1}$, which is an approximate value chosen based on frequencies for

frustrated translation of a few hundred wave numbers (based upon frequency projections performed for frustrated translation on the Ni(111) surface, following the method described previously [23]). Though the pre-factor is estimated, the correction (M_{Int}/M_{f_s}) is still applied. The barrier for diffusion is either calculated via DFT or estimated, as detailed in Table 6.

The reverse rate coefficient for inter-facet diffusion takes the form.

$$k_{-if_{s,i}} = k_{if_{s,i}} \exp \left(\frac{\Delta G_{if_{s,i}}}{RT} \right) \left(\frac{C_{Tf_s}}{C_{Tf_i}} \right), \quad (11)$$

where $\Delta G_{if_{s,i}}$ is the change in Gibbs free energy for diffusion of a mole of species i from facet f_s to facet f_i . Note that the lack of a standard state number of binding sites per species correction in Eq. 11 is a result of the same standard state for each surface facet in the model.

3 Results and Discussion

3.1 Estimation of Fractional Abundance of Each Surface Facet

In order to account for differences in the relative abundance of each surface facet, the fraction of each surface facet as a function of particle size is calculated as an input for the kinetic model. The equilibrium shape of the nickel particle is assumed to be a truncated octahedron with Ni(111) and Ni(100) facets. The relative stability of these facets is used to determine the relative abundance of the binding sites, with the boundaries between the facets being treated as Ni(211) step edges. The resulting surface fraction of each facet is shown in Fig. 3. For an approximately 7 nm particle size, the fraction of each surface facet is found to be 0.74, 0.15, and 0.11 for Ni(111), Ni(100), and the Ni(211) surfaces, respectively. In this work, comparisons are made to the SMR experimental data sets of Xu and Froment [13] as well as those of Wei and Iglesia [12]. The ~ 7 nm nickel particle size is consistent with the catalyst particles in the experiments of Wei and Iglesia. The catalyst particle size in the experiments of Xu and Froment is not provided and is assumed to equal that of Wei and Iglesia’s nickel catalyst for the calculations in this work.

A comparison of the truncated octahedron-predicted fractions to the results of full Wulff constructions, up to a particle size of approximately 10 nm, is shown in Fig. 3. The Wulff construction data, which are considered a more accurate prediction of equilibrium particle shape, were obtained via personal communication with A. Hellmann from calculations conducted to support the investigation of particle size effect in the oxygen reduction reaction [35]. The truncated octahedron data agree reasonably well with

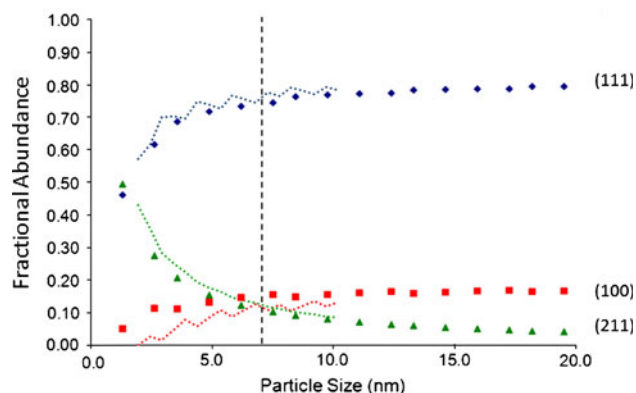


Fig. 3 Fraction of each surface facet versus particle size for the Ni(111) facet, Ni(100) facet, and step edges, which are modeled as the Ni(211) surface in this study. Particle size used in the present study, 7 nm, is indicated by *dashed vertical line* for reference. Data are computed using a truncated octahedron model and are compared to full Wulff construction data (*dotted lines*), where available (data used for previously published results [35] provided via personal communication with A. Helmann)

the data from full Wulff constructions, particularly for the Ni(111) surface and the (211) nickel step edge. While there exists some discrepancy for the Ni(100) surface, the two methods produce better agreement with increasing particle size. The truncated octahedron method is applied in the present work because of its computational ease (algebraic equations) and reasonable accuracy relative to full Wulff constructions, particularly for nanoparticles with diameters in excess of 5 nm.

There are eight hexagonal (111) facets and six square (100) facets on the surface of a truncated octahedron. Half of the edges on the surface are between a square face and a hexagonal face, while the other half are between two hexagonal faces. Thus, treating the edge atoms as a (211) step edge (as described above in computational methods), all step edge atoms border at least one (111) facet and one-half of the step edge atoms border a (100) facet. This information is useful in defining the ratio of interfacial sites to total binding sites of a given facet term in the rate coefficient for inter-facet diffusion. For example, for the interface between the (111) facet and (211) step edge, all (211) step edge sites border a (111) site, so the ratio of interfacial sites to total (211) step edge binding sites is 1. The ratio of interfacial sites to (111) sites is calculated by multiplying the previous ratio, 1, by the ratio of the fraction of (211) sites to the fraction of (111) sites. For a 7 nm nickel particle, the result is 0.15 (i.e., 15% of the (111) binding sites border a step edge site). A similar procedure is carried out for the interface between the (100) facet and the (211) step edge sites. The resulting ratio of interface to (211) sites is 0.5, while the ratio of interface sites to (111) sites is 0.37.

Table 1 DFT-predicted species binding energies (kJ/mol) on Ni(111), Ni(100), and Ni(211)

Species	Ni(111)	Ni(100)	Ni(211)
CH ₃ *	−137	−137	−171
CH ₂ *	−335	−356	−347
CH*	−576	−636	−600
CH* (0.25 ML) ^a	—	−635	—
CH* (0.5 ML) ^a	—	−595	—
C*	−613	−749	−706
C* (0.25 ML) ^a	—	−727	—
C* (0.5 ML) ^a	—	−692	—
H*	−255	−255	−257
H ₂ O* ^d	−2	−2 ^c	−2 ^c
OH*	−294	−314	−316
O*	−496	−527	−513
CO*	−151	−148	−154
CHO*	−164	−213	−176
COH* ^b	−191	−218	−177
COOH*	−217	—	—
CO ₂ * ^d	3	—	3 ^c

^a Species is corrected for coverage-dependent effects. See discussion of coverage-dependent binding energies in Sect. 3.4 below

^b COH* binding energy is relative to CHO(g)

^c Binding energy is assumed to equal the DFT-computed binding energy for this species on the (111) surface facet

^d Ni(111) binding energy is taken from previously published value for that surface [23]

3.2 Species Thermochemistry

Density functional theory calculations are used to predict the binding energies and electronic reaction energies for the surface intermediates and reactions shown in Fig. 1. Binding energies for the species of interest are computed on the Ni(111), Ni(211), and Ni(100) surface facets. The resulting binding energies of the surfaces of interest are shown in Table 1. Because the H₂O*, COOH*, and CO₂* are not sensitive species in the mechanism and do not participate in any rate-limiting reactions, the binding energy obtained previously for these species on Ni(111) [23] is used in the present study.

In general, species are found to be more tightly bound on the (211) and (100) surfaces than on the (111) surface. In particular, carbon is significantly stabilized relative to the (111) surface because of increased coordination of the carbon atom along the step edge on the (211) surface and in a four-fold hollow binding site on the (100) surface. The Ni(100) binding energy results are generally consistent with available experimental data. The binding energy is predicted to be approximately the same for hydrogen on the

(111) and (100) surfaces, which is consistent with experimental observations [39, 40]. The binding energy for CO is predicted to decrease slightly from the (111) to (100) surfaces, which is consistent with experiment that shows a decrease of 8 kJ/mol at similar coverages [41]. Finally, the binding energy of oxygen is predicted to increase on the (100) surface relative to the (111) surface. Experimental results agree with this trend; however, there is more error for the oxygen binding energy than for CO* or H*, as DFT under-predicts the change in O* binding energy between the two surfaces by approximately 40 kJ/mol [42].

When obtaining thermodynamic quantities such as heats of reaction and entropies of reaction, the vibrational frequencies obtained previously for the Ni(111) surface [23] are used for the corresponding species on the Ni(100) and Ni(211) surface. Thus, the computed entropies of reaction are the same for a given reaction, regardless of the surface facet upon which it is occurring. Likewise, the zero-point energy and thermal corrections used in obtaining heats of reaction from the electronic reaction energies are the same for a given reaction, regardless of surface. The computed heats of reaction are a function of the surface facet upon which the reaction is occurring, but only because the electronic energies of reaction were computed for the reactions on each surface facet.

The heats of adsorption for species on the Ni(111) surface are adjusted using available experimental data and the computed heats of reaction for surface reactions, as described previously. Next, heats of adsorption for the Ni(211) and Ni(100) surfaces are estimated by adding the difference in the computed binding energy between the Ni(211) or Ni(100) and the Ni(111) surface to the experimentally-adjusted heat of adsorption for a species on the Ni(111) surface. The resulting heats of adsorption for each species/surface are shown in Table 2 and the corresponding heats and entropies of reaction are shown in Table 3.

First-order saddle point searches are performed to obtain transition state geometries for dissociative methane adsorption and carbon-containing intermediates species oxidation (i.e., CO* formation from C* to O*, CHO* formation from CH* to O*, and COH* formation from C* to OH*). Where available, reaction barriers for reactions in the mechanism that are not evaluated in the present study are taken from previously published values, as indicated in the tables. The previously published values were calculated in Dacapo, rather than VASP. In all cases, the RPBE functional was employed. Dacapo makes use of ultra-soft pseudopotentials to describe the role of core electrons while VASP employs projector-augmented wave potentials. As a result, binding energy and reaction energy predictions may differ between the two packages. In the present work, the thermochemical landscape for the (111) surface is computed in VASP (rather than using values

Table 2 Experimentally-adjusted heats of adsorption (kJ/mol) at 575 °C

Species	Ni(111)	Ni(100)	Ni(211)
CH ₃ *	−180	−180	−213
CH ₂ *	−374	−396	−387
CH*	−568	−627	−591
CH* (0.25 ML) ^a	–	−626	–
CH* (0.5 ML) ^a	–	−586	–
C*	−591	−726	−683
C* (0.25 ML) ^a	–	−704	–
C* (0.5 ML) ^a	–	−669	–
H*	−268 ^c	−268	−270
OH*	−275	−296	−298
O*	−464 ^c	−495	−480
CO*	−124 ^c	−122	−128
CHO*	−192	−242	−204
COH* ^b	−215	−242	−201

^a Species is corrected for coverage-dependent effects. See discussion of coverage-dependent binding energies in Sect. 3.4 below

^b COH* heat of adsorption is relative to CHO(g)

^c Heat of adsorption is calculated from experimental quantity at 25 °C, which is then corrected to 575 °C using DFT-computed frequencies

previously calculated in Dacapo) to provide greater thermodynamic consistency with the VASP-predicted thermochemistry for the (211) and (100) surfaces presented here. In some cases, activation energies computed in Dacapo are used to compute the kinetics of reactions in the model (such as for CH_x* and H₂O* dissociation); however, all reactions determined to be potentially rate-limiting were computed in VASP to avoid any potential inconsistency. It should be noted, however, that in a test case, the activation energies for CH₃* dissociation to CH₂* and H* on the Ni(111) surface predicted by the two software packages were found to agree well, within 2 kJ/mol. Kinetic parameters for methane activation and the three investigated oxidation pathways (direct CO* formation through C* + O*, as well as formation of CO* through CHO* and COH* intermediates) are shown in Table 4.

Dissociative methane adsorption is found to have the lowest barrier on the Ni(211) surface, with a computed zero-point-corrected electronic barrier of 75 kJ/mol, which is in good agreement with the value of approximately 80 kJ/mol previously reported by Bengaard, et al. [21]. The methane activation barriers on the Ni(100) and Ni(111) surface facets are found to be 98 kJ/mol and 111²³ kJ/mol, respectively. The activation barrier for the addition of C* and O* to form CO* is also reduced on the Ni(211) surface relative to the Ni(111) surface, decreasing from 199 kJ/mol to 157 kJ/mol. These results are in agreement with

Table 3 Heats and entropy of reaction for SMR over multi-faceted Ni at 575 °C

Reactions	ΔH_{rxn} (kJ/mol)			$\Delta S_{\text{rxn}}^{\text{c}}$ (J/mol-K)
	Ni(111) [23]	Ni(100) ^d	Ni(211)	
$\text{H}_2(\text{g}) + 2^* = \text{H}^* + \text{H}^*$	−94	−94	−97	−132
$\text{H}_2\text{O}(\text{g}) + ^* = \text{H}_2\text{O}^*$	−12	−12	−12	−86
$\text{CO}(\text{g}) + ^* = \text{CO}^*$	−124	−122	−128	−135
$\text{CH}_4(\text{g}) + 2^* = \text{CH}_3^* + \text{H}^*$	1	1	−34	−130
$\text{CO}_2(\text{g}) + ^* = \text{CO}_2^*$	−26	—	−26	−91
$\text{CH}_3^* + ^* = \text{CH}_2^* + \text{H}^*$	6	−15	26	−2
$\text{CH}_2^* + ^* = \text{CH}^* + \text{H}^*$	−32	−70	−45	−15
$\text{CH}^* + ^* = \text{C}^* + \text{H}^*$	53	−22	−17	−3
$\text{H}_2\text{O}^* + ^* = \text{OH}^* + \text{H}^*$	−27	−47	−51	−60
$\text{OH}^* + ^* = \text{O}^* + \text{H}^*$	−20	−30	−16	−18
$\text{C}^* + \text{O}^* = \text{CO}^* + ^*$	−152	17	−47	33
$\text{C}^* + \text{OH}^* = \text{COH}^* + ^*$	−66	63	63	16
$\text{CH}^* + \text{O}^* = \text{CHO}^* + ^*$	31	72	58	18
$\text{CHO}^* + ^* = \text{CO}^* + \text{H}^*$	−130	−77	−122	12
$\text{COH}^* + ^* = \text{CO}^* + \text{H}^*$	−106	−77	−125	−1
$\text{CO}^* + \text{OH}^* = \text{COOH}^* + ^*^{\text{a}}$	77	—	—	−37
$\text{COOH}^* + ^* = \text{CO}_2^* + \text{H}^*^{\text{a}}$	−71	—	—	65
$\text{CO}^* + \text{O}^* = \text{CO}_2^* + ^*^{\text{b}}$	26	—	41	47
$\text{CO}^* + \text{CO}^* = \text{CO}_2^* + \text{C}^*^{\text{a}}$	178	—	—	14

^a This water–gas shift reaction is included only on the Ni(111) surface

^b This water–gas shift reaction is included only on the Ni(111) and Ni(211) surface facets

^c Frequencies obtained previously for Ni(111) are used for all surfaces in present study, resulting in surface-independent entropies

^d All heats of reaction for the Ni(100) surface are computed at the default computational coverage of 1/8 ML. Coverage-dependent effects for C* and CH* are not shown. These effects are calculated in the microkinetic model using the data in Table 2 and the method described in Sec. 3.4 below

Table 4 Zero-point-corrected activation energies and corresponding pre-factors at 575 °C for SMR reactions investigated in the present study

Reactions	E_{o} (kJ/mol)			A (s^{-1}) ^a		
	Ni(111) [23]	Ni(100)	Ni(211)	Ni(111) [23]	Ni(100)	Ni(211)
$\text{CH}_4(\text{g}) + 2^* = \text{CH}_3^* + \text{H}^*$	111	98	75	7.3×10^6	8.1×10^6	7.6×10^6
$\text{C}^* + \text{O}^* = \text{CO}^* + ^*$	199	200	157	4.2×10^{14}	7.1×10^{12}	1.0×10^{13}
$\text{C}^* + \text{OH}^* = \text{COH}^* + ^*$	124	152	146	2.3×10^{13}	6.8×10^{12}	7.0×10^{12}
$\text{CH}^* + \text{O}^* = \text{CHO}^* + ^*$	128	193	132	1.5×10^{13}	8.7×10^{12}	6.4×10^{12}
$\text{COH}^* + ^* = \text{CO}^* + \text{H}^*$	81	88	40	2.0×10^{12}	9.9×10^{12}	3.8×10^{12}

^a Calculated using $(k_{\text{B}}T/h)[q^{\text{TS}}/\Pi q_i]$, without standard state correction or concentration of sites term

previous calculations and the general trend expected for dissociative methane adsorption and CO* formation on stepped surfaces [21, 43]. However, the barriers for CHO* and COH* formation are found to increase slightly on the Ni(211) surface relative to the Ni(111) surface. The CHO* and COH* formation reactions also exhibit larger activation barriers on the Ni(100) surface; however, the increase is more significant for CHO* formation, increasing from 128 kJ/mol on Ni(111) to 193 kJ/mol on Ni(100).

Comparisons of the thermochemistry (at 575 °C) and reaction barriers of the pathways investigated in the present study on the Ni(100) and Ni(211) surfaces are shown in Figs. 4 and 5, respectively. While some activation barriers for carbon-containing intermediate species oxidation do increase, the significant stabilization of the intermediate species on the Ni(100) and Ni(211) surfaces leads to lower transition state energies relative to the energy of the gas phase reactants. On Ni(100), the lowest-energy pathway is

Table 5 Fractional surface coverage of vacant sites and selected reaction intermediates at $\sim 5\%$ CH_4 conversion, 575°C , $p = 10$ bar, steam:methane = 2.5

Species	Ni(111)	Ni(100)	Ni(211)
Vacant	7.8×10^{-1}	3.6×10^{-1}	6.8×10^{-1}
C^*	1.8×10^{-7}	3.0×10^{-1}	7.5×10^{-2}
CH^*	1.2×10^{-4}	2.2×10^{-1}	2.8×10^{-3}
H^*	1.9×10^{-1}	7.7×10^{-2}	1.9×10^{-1}
O^*	1.1×10^{-3}	4.0×10^{-2}	1.1×10^{-2}
OH^*	1.3×10^{-4}	1.1×10^{-3}	2.8×10^{-3}
CO^*	1.9×10^{-2}	6.7×10^{-3}	3.0×10^{-2}

Table 6 Diffusion barriers (kJ/mol) on the multi-faceted nickel surface

Species	Ni(111) to Ni(211)	Ni(211) to Ni(100)
CH_3^*	25 ^a	25 ^a
CH_2^*	25 ^a	25 ^a
CH^*	46	119
C^*	50	196
H^*	13	13 ^b
H_2O^*	0.3	0.3 ^b
OH^*	25 ^a	19
O^*	48	61
CO^*	10	3
CHO^*	13	13 ^b
COH^*	25 ^a	25 ^a

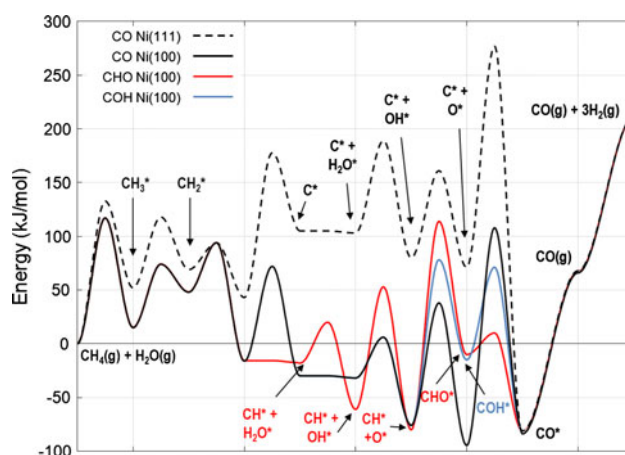
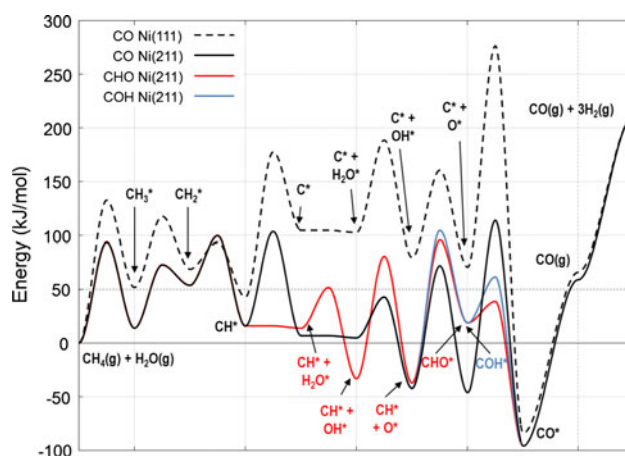
Diffusion barriers are calculated on the larger facet across which molecules must diffuse (i.e., Ni(111) and Ni(100)). Ni(111) values are taken from barriers calculated for previously published results [23]. Ni(100) values are calculated in the present study and are defined as the difference in adsorption energies between a bridge binding site and a hollow binding site on the Ni(100) surface

^a Diffusion barrier is not explicitly calculated and is assumed to equal 25 kJ/mol

^b Diffusion barrier is not calculated and is assumed to equal the barrier calculated for the Ni(111) surface

through the COH^* intermediate, followed by direct formation of CO^* from C^* to O^* . However, as shown in Fig. 4, the effective barrier for CO^* formation from C^* to OH^* through COH^* is only 20 kJ/mol less than the barrier for CO^* formation from C^* to O^* . Also, as mentioned previously, the calculated O^* energy disagrees with experimental values by 40 kJ/mol, introducing error that makes it less clear which C–O coupling reaction will be faster.

Like the Ni(100) surface, many intermediate species on Ni(211) are significantly stabilized relative to the Ni(111) surface. As shown in Fig. 5, the lowest (electronic) energy pathway on the Ni(211) surface is through the CHO^*

**Fig. 4** Electronic energies and activation barriers of SMR pathways [relative to $\text{CH}_4(\text{g}) + \text{H}_2\text{O}(\text{g})$] on the Ni(100) surface compared to the pathway through $\text{C}^* + \text{O}^* \rightarrow \text{CO}^*$ on Ni(111). Some species labels are omitted to simplify notation**Fig. 5** Electronic energies and activation barriers of SMR pathways [relative to $\text{CH}_4(\text{g}) + \text{H}_2\text{O}(\text{g})$] on the Ni(211) surface compared to the pathway through $\text{C}^* + \text{O}^* \rightarrow \text{CO}^*$ on Ni(111). Some species labels are omitted to simplify notation

intermediate, followed by the formation of COH^* from C^* to OH^* and the direct formation of CO^* from C^* to O^* . However, for the Ni(100) surface and particularly the Ni(211) surface, the differences between the investigated pathways are small, suggesting a kinetic model will be most useful in discerning the most favorable reforming pathways.

The results of our DFT calculations indicate that the Ni(100) and Ni(211) will provide an enhanced kinetic effect in the SMR reaction because of a significant stabilization of reaction intermediates as well as a reduction of the barrier to methane chemisorption and some carbon-containing intermediate species oxidation barriers. To gain a better understanding of the competition between these pathways, we next include these thermochemical and

kinetic parameters in a kinetic model that will allow for flux and sensitivity analysis as well as comparison to experiment.

3.3 Microkinetic Modeling

The reactions shown in Fig. 1 are included in a microkinetic model, combining the thermochemistry listed in Table 3 with the kinetic parameters listed in Table 7. In addition, two diffusion reactions are included for each species to account for inter-facet diffusion from the Ni(111) to the Ni(211) surface and from the Ni(211) to the Ni(100) surface. Exceptions to this are COOH*, which has

no inter-facet diffusion reactions because it is only included on the Ni(111) surface, and CO₂*, which has one inter-facet diffusion reaction between the Ni(111) and Ni(211) surfaces). The heats of diffusion are defined from the values listed in Table 2 and the estimated barriers for diffusion are listed in Table 6. The WGS reactions are studied using previously published kinetic parameters. As detailed in Table 7, the complete set of WGS reactions shown in Fig. 1 are investigated on the Ni(111) surface using previously computed values [23]. Only the most facile reaction on the (111) facet, the CO* + O* → CO₂* reaction, is investigated on the (211) facet using a previously reported activation barrier [44].

Table 7 Arrhenius parameters for SMR kinetic model over multi-faceted Ni

Reactions	Ea (kJ/mol)			A ^a		
	Ni(111)	Ni(100)	Ni(211)	Ni(111)	Ni(100)	Ni(211)
1: H ₂ (g) + 2* = H* + H* ^b	11	11	11	1.0 × 10 ³	8.9 × 10 ²	1.0 × 10 ³
2: H ₂ O(g) + * = H ₂ O*	0	0	0	8.6 × T ^{0.5}	8.6 × T ^{0.5}	8.6 × T ^{0.5}
3: CO(g) + * = CO*	0	0	0	6.9 × T ^{0.5}	6.9 × T ^{0.5}	6.9 × T ^{0.5}
4: CH ₄ (g) + 2* = CH ₃ * + H*	133	117	94	3.0 × 10 ²	2.8 × 10 ²	3.0 × 10 ²
5: CO ₂ (g) + * = CO ₂ *	0	–	0	5.5 × T ^{0.5}	–	5.5 × T ^{0.5}
6: CH ₃ * + * = CH ₂ * + H* ^c	66	59	59	4.7 × 10 ¹³	4.7 × 10 ¹³	4.7 × 10 ¹³
7: CH ₂ * + * = CH* + H* ^c	25	46	46	8.3 × 10 ¹²	8.3 × 10 ¹²	8.3 × 10 ¹²
8: CH* + * = C* + H* ^c	135	88	88	2.1 × 10 ¹⁴	2.1 × 10 ¹⁴	2.1 × 10 ¹⁴
9: H ₂ O* + * = OH* + H* ^c	87	38	38	1.3 × 10 ¹¹	1.3 × 10 ¹¹	1.3 × 10 ¹¹
10: OH* + * = O* + H* ^c	82	114	114	8.5 × 10 ¹²	8.5 × 10 ¹²	8.5 × 10 ¹²
11: C* + O* = CO* + *	206	202	160	3.3 × 10 ¹⁹	3.4 × 10 ¹⁷	4.9 × 10 ¹⁷
12: C* + OH* = COH* + *	126	154	147	9.8 × 10 ¹⁷	3.3 × 10 ¹⁷	2.7 × 10 ¹⁷
13: CH* + O* = CHO* + *	131	195	134	7.6 × 10 ¹⁷	3.9 × 10 ¹⁷	2.5 × 10 ¹⁷
14: CHO* + * = CO* + H* ^b	20	20	20	9.2 × 10 ¹²	9.2 × 10 ¹²	9.2 × 10 ¹²
15: COH* + * = CO* + H* ^d	85	93	43	3.6 × 10 ¹²	2.1 × 10 ¹³	6.1 × 10 ¹²
16: CO* + OH* = COOH* + * ^e	111	–	–	3.2 × 10 ²⁰	–	–
17: COOH* + * = CO ₂ * + H* ^e	97	–	–	1.0 × 10 ¹⁶	–	–
18: CO* + O* = CO ₂ * + * ^e	149	–	142 ^f	3.2 × 10 ²⁰	–	3.2 × 10 ²⁰
19: CO* + CO* = CO ₂ * + C* ^e	326	–	–	3.2 × 10 ¹⁷	–	–

Unless otherwise shown, Arrhenius pre-factors and activation energies are temperature-independent, regressed over the range 500–575 °C. Values for the Ni(111) surface are computed from previously published values [23]. Pre-factors for non-activated molecular adsorption are shown with the appropriate temperature dependence. Pre-factors for all other adsorption reactions contain a standard state correction calculated at 575 °C

^a All pre-factors are in MKS units of length/number · s (e.g., m/s for reaction 1 and m²/mol·s for reaction 11)

^b The activation energy and pre-exponential factor for this reaction is taken from the results obtained previously for the Ni(111) surface and is assumed to be the same for each surface in the model. The pre-exponential factor is corrected for the differing number of binding sites per unit area on the surfaces of interest

^c The activation energy for the Ni(211) surface is taken from previously published values by Bengaard, et al. (un-regressed) [21]. The activation energy for the reaction on the Ni(100) surface is assumed to equal the activation energy on the Ni(211) surface. The pre-exponential factor obtained previously for the Ni(111) surface is used for all surfaces

^d Because the kinetic model shows sensitivity to this reaction's barrier on the Ni(100) surface, that barrier was computed. The barrier and pre-factor on the Ni(211) surface are assumed to equal the parameters obtained previously for the Ni(111) surface

^e The Arrhenius pre-factor is estimated as $k_{\text{B}}T/h$, with appropriate unit corrections

^g The activation barrier for this water–gas shift surface reaction is taken from a value previously published by Jiang, et al. [44]

3.4 Coverage-Dependent Binding Energies

At the high-temperatures investigated in the present work, coverage of species is generally low (Table 5) because of significant entropic effects. However, C* and CH* are found to have sufficiently large binding energies on the Ni(100) surface to result in coverage well in excess of the default computational coverage for the Ni(100) surface of 1/8 monolayer (ML). At the conditions described below for the CSTR formulation, the coverage of C* is predicted to be greater than 0.95 ML. Consequently, the binding energies of C* and CH* are corrected for coverage-dependent effects using the data listed in Table 2. The species H* is also found to exist at relatively high coverages under certain conditions (such as high conversion where hydrogen partial pressure is large); however, the binding energy of H* is not a strong function of coverage and therefore coverage-dependent effects are ignored. The Ni(100) binding energies for C* and CH* are assumed to be constant at coverages less than 1/8 ML. For the range from 1/8 to 1/4 ML and 1/4 to 1/2 ML, the binding energy is linearly interpolated between the computed endpoints. The coverage-dependent binding energies are implemented by adjusting the heat of reaction for all reactions involving C* and/or CH* as appropriate depending on the species' coverages at the time step of interest. For both C* and CH*, the Ni(100) binding energy is found to decrease with increasing coverage. As a result, the coverage of each species is found to decrease as a result of the introduction of coverage-dependent binding energies. For example, the fractional coverage of C* on Ni(100) is predicted to decrease from 0.95 with no coverage-dependence to 0.30 ML when coverage-dependent effects are included. Under the conditions examined in the present study, no species surface coverage was found to exceed 0.5 ML, so corrections above this coverage are not implemented. Note that no additional adsorbate–adsorbate interactions are included in the present model.

3.5 CSTR Formulation for Flux and Sensitivity Analysis

We investigate the microkinetic model using a CSTR to quickly investigate parallel competing pathways on the catalyst surface (both the competition between individual surface facets and the competition among parallel reactions on a given surface facet). The kinetics of SMR are investigated at 575 °C and 10 bar total pressure with a H₂O:CH₄ ratio of 2.5 and a reactor residence time of 2 s, which with the present model corresponds to approximately 5% methane conversion. In the simulation, there are 1.83×10^{-6} total moles of nickel binding sites. The fractional abundance of each type of site is taken from the surface facet analysis presented above.

The steady state coverage of vacant sites and selected reaction intermediates for each surface facet is shown in Table 5. The Ni(111) surface coverage is consistent with values obtained in our previous investigation of this surface with the surface being mostly vacant and the most abundant reaction intermediate being H*, with a predicted fractional coverage of approximately 0.19 and a fraction of vacant sites equal to 0.78. The Ni(100) surface is predicted to be more concentrated with surface species, with a fraction of vacant sites equal to 0.36 after coverage-dependent effects for C* and CH* (the most abundant reaction intermediates on this surface) are included. The Ni(211) surface is also found to be more concentrated with surface species than the Ni(111) surface; however, most intermediates are predicted to be less stable on this surface than on the Ni(100) surface, which results in a larger fractional coverage of vacant sites at 0.68. The most abundant reaction intermediate on the Ni(211) surface is predicted to be H* followed by C*.

The most active surface facet for dissociative methane adsorption is predicted to be the stepped Ni(211) surface, accounting for 95% of the methane adsorption on the catalyst surface. The subsequent CH_x* species dissociations are found to occur quickly at step sites as well as on the Ni(100) surface. The Ni(211) surface is predicted to be the preferred surface for adsorbed water dissociation to OH* and H*, while the final dissociation of OH* to O* and H* is predicted to be more facile on the Ni(111) surface. It should be noted, however, that the current kinetic parameters for water dissociation on the Ni(100) surface are approximated as being equal to the parameters on the Ni(211) surface; thus, predictions of dissociation products of H₂O* on the Ni(100) surface are uncertain. And, as noted above, the computed O* energy on Ni(100) surface used here differs significantly from the experimental number. While the H₂O dissociation kinetics are not sensitive parameters in the model, the stability of the O* intermediate can effect C–O coupling rates.

The Ni(211) and Ni(100) surfaces are predicted to be the most active surfaces for the oxidation of carbon-containing intermediates. Each of the oxidation reactions included in the microkinetic model are found to be active pathways on the Ni(211) surface. At the conditions studied in the CSTR, approximately 27% of the adsorbed methane is converted to CO* through the direct-addition of C* and O* on the Ni(211) surface. Approximately 26% of the adsorbed methane is found to be converted to CO* through the reaction of C* and OH* to form COH* on Ni(211), followed by 20% through the reaction CH* and O* to form CHO* also on Ni(211). Thus, the nickel step edge is predicted to be responsible for roughly 75% of the carbon-containing species' oxidation at these conditions. The primary oxidation reaction on the Ni(100) surface is predicted

to be the formation of COH^* from C^* and OH^* , accounting for the oxidation of 21% of the adsorbed methane. The pathways through the direct formation of CO^* from C^* and O^* and the formation of CHO^* from CH^* and O^* on $\text{Ni}(100)$ are less active, accounting for the oxidation of 1% and 2% of the adsorbed methane, respectively. The remainder of the flux (3%) is accounted for through the formation of CHO^* on $\text{Ni}(111)$.

Discrete sensitivity analysis is performed to determine the rate-limiting reactions at the present conditions by adjusting the Arrhenius pre-factor up/down by a factor of 100 while observing changes in total methane conversion relative to the unperturbed reference case. This perturbation is equivalent to decreases/increases in the activation energy of approximately 30 kJ/mol at 575 °C. The overall rate of methane conversion is predicted to be most sensitive to dissociative methane adsorption (primarily at the nickel step edge) as well as the oxidation class of reactions, C^* and CH^* reacting with O^* and OH^* (primarily at the nickel step edge and on the $\text{Ni}(100)$ surface). The dissociative methane adsorption reaction is found to be more sensitive to negative perturbations than positive, while the opposite is true for the oxidation reactions.

3.6 Comparison to Available Experimental Data

The microkinetic model is also studied in a plug-flow reactor model to investigate methane conversion as a function of space time for comparison to available experimental data. To compare with the experimental results of Xu and Froment [13], the system is modeled over a temperature range of 500–575 °C, at a pressure of 10 bar, a $\text{H}_2\text{O}:\text{CH}_4$ ratio of 3, and a $\text{H}_2:\text{CH}_4$ ratio of 1.25. The surface area of the catalyst is modeled as $7.2 \text{ m}^2/\text{g}_{\text{cat}}$, a reduction from the $9.3 \text{ m}^2/\text{g}_{\text{cat}}$ cited by Xu and Froment for fresh catalyst, to account for catalyst deactivation reported in their study. The void fraction of the catalyst and diluent is modeled as 0.528, per the referenced study. The concentration of binding sites and fractional coverage of each surface facet used for the CSTR analysis are assumed to be applicable here. Measured fractions of sites, such as the ratio of step sites to terrace sites, were not reported by Xu and Froment.

The computational results obtained in this study are compared to the experimental results in Fig. 6. While the multi-faceted kinetic model is slow relative to observed reforming rates, it represents a significant improvement over the previously published $\text{Ni}(111)$ model. As expected, the presence of additional surface facets in the multi-faceted model results in considerably faster kinetics, as is shown in Fig. 7b, where the multi-faceted model-predicted conversion at 575 °C is compared to the predicted conversion of the previously published $\text{Ni}(111)$ model.

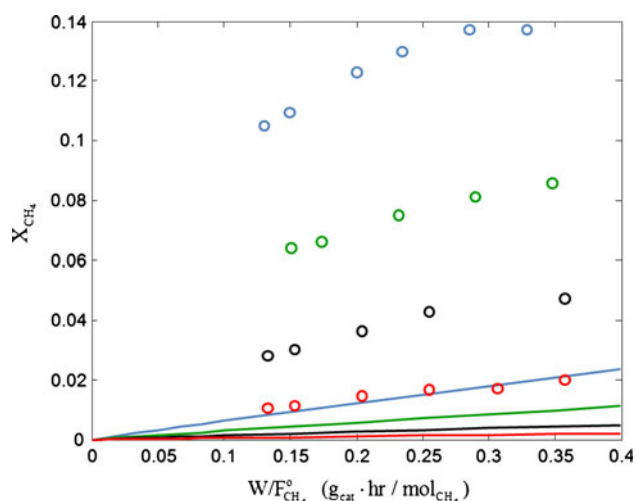


Fig. 6 Comparison of computed conversion of methane versus space time (solid lines) in an ideal PFR to experimental results of Xu and Froment (hollow circles) at (in order from bottom to top for both the experimental and predicted data sets) 500, 525, 550, and 575 °C

Dissociative methane adsorption has been demonstrated to be the rate-limiting SMR step at high temperatures by Wei and Iglesia [12]. As shown in Fig. 7a, the present model predicts the forward rate of dissociative methane adsorption reasonably well, showing a considerable improvement over the $\text{Ni}(111)$ model because of the importance of step sites in dissociative methane adsorption. The predicted dissociative methane adsorption rates from the multi-faceted model are computed at a fractional abundance of sites for the (111), (100) and (211) surfaces of 0.74, 0.15, and 0.11, respectively (chosen based on the particle size cited by Wei and Iglesia, 6.7 nm, and the fractional abundance of binding sites analysis presented above). In the calculation, the fraction of vacant sites is computed to be 0.75, 0.50, and 0.65 for the (111), (100), and (211) surfaces, respectively, at Xu and Iglesia's conditions.

However, despite the accurate prediction of Wei and Iglesia's rate of dissociative methane adsorption by the model, the overall rate of SMR (Figs. 6, 7b) is under-predicted. Based on the sensitivity analysis presented above for the CSTR model, the carbon-containing intermediate species oxidation reactions at the nickel step edge and on $\text{Ni}(100)$ as well as dissociative methane adsorption at the nickel step edge are the primary sensitive reactions in the mechanism. Thus, the reasonably accurate prediction of dissociative methane adsorption rates but under-prediction of overall methane conversion rates suggests that one or more oxidation rates may be under-predicted by the current model. The under-prediction of the overall methane conversion rate is not necessarily (and likely not) solely a result of under-predicted oxidation rates. For example, the total fraction of step sites is approximated in the current

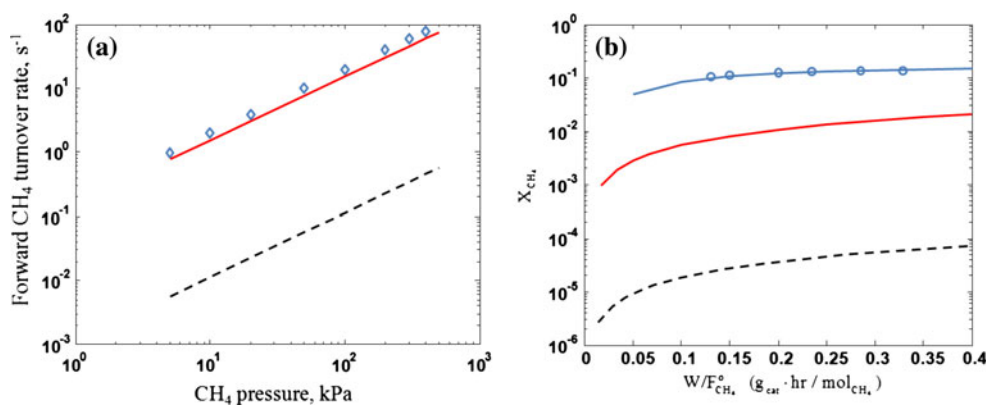


Fig. 7 Forward CH_4 turnover rate versus CH_4 partial pressure at 600 °C **a** as observed by Wei and Iglesia (open diamonds), predicted by the present model (line), and predicted by the previously published Ni(111) model (dashed line). Methane conversion versus space time

at 575 °C **b** as observed/ modeled by Xu and Froment (open circles on line), predicted by the present model (line), and predicted by the previously published Ni(111) model (dashed line)

model, and a higher fraction of step sites and/or Ni(100) sites on the actual catalyst would result in faster reforming rates. However, the predicted rate-limitation of the C–O addition reactions at temperatures where it is not observed experimentally [12] is an indication that these rates are under-predicted to some degree by the present model.

The degree of rate-limitation between dissociative methane adsorption and carbon-containing intermediate species oxidation is predicted to be a function of temperature. The free energy barriers for dissociative methane adsorption and the formation of CO^* from C^* and O^* are found to increase and decrease, respectively, with increasing temperature. Therefore, at low temperatures, the oxidation reactions are predicted to be rate-limiting (with a lower fraction of the total flux through $\text{C}^* + \text{O}^*$) while dissociative methane adsorption is predicted to be rate-limiting at high temperatures (with a higher fraction of the total flux through $\text{C}^* + \text{O}^*$). This result is consistent with previous computations for these reactions [18] as well as the experimental observation [12] that dissociative methane adsorption is rate-limiting under high temperature conditions. As shown Fig. 8, the dissociative methane adsorption transition state is predicted to be the highest point in the free energy landscape (the most rate-limiting) on the nickel step edge at high temperatures; however, not until higher temperatures than those where Wei and Iglesia found methane adsorption rate control (we predict a transition at approximately 800 °C, while Wei and Iglesia observe dissociative methane adsorption rate limitation at temperatures near 600 °C). These results present a general picture that at low temperatures, the oxidation of carbon-containing intermediate species is rate-determining, followed by a transition region of intermediate temperatures where there exists varying degree of rate control between dissociative methane adsorption and the oxidation

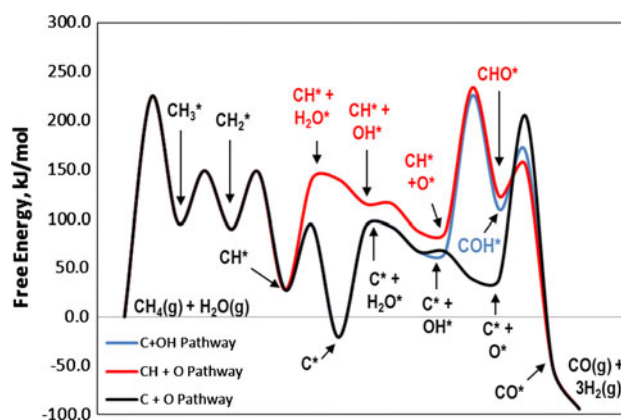


Fig. 8 Vertical free energy (kJ/mol) diagram for SMR through $\text{C}^* + \text{O}^*$ (black), $\text{CH}^* + \text{O}^*$ (red), and $\text{C}^* + \text{OH}^*$ (blue) on Ni(211) at 1000 °C on Ni(211) with a standard state pressure of 1 bar and a standard state surface species coverage of 1 ML. Some species labels are omitted to simplify notation

reactions, followed by a high-temperature regime where dissociative methane adsorption reaction is the rate-determining step. A similar temperature-dependent transition in rate-limiting steps has been suggested for SMR over ruthenium catalyst [45].

The transition state free energies of other carbon-species oxidation reactions such as COH^* and CHO^* formation are not found to be strong functions of temperatures. Thus, at high temperatures, the lowest-energy pathway is predicted to be through the direct reaction of C^* and O^* to form CO^* on the Ni(211) surface. However, at lower temperatures as shown in Fig. 9, the primary reforming pathway is predicted to shift from direct formation of CO^* , with the lowest-energy pathways predicted to be through the hydrogen-mediated pathways of COH^* and CHO^* rather than direct formation of CO^* , particularly the formation of COH^* on the Ni(100)

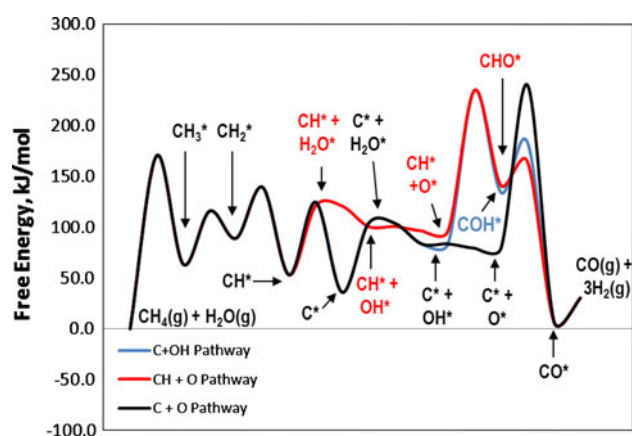


Fig. 9 Vertical free energy (kJ/mol) diagram for SMR through $C^* + O^*$ (black), $CH^* + O^*$ (red), and $C^* + OH^*$ (blue) on Ni(211) at 500 °C on Ni(211) with a standard state pressure of 1 bar and a standard state surface species coverage of 1 ML. Some species labels are omitted to simplify notation

surface. However, at these lower temperatures, the oxidation pathways are found to be rate-limiting and the flux through the pathways is not predicted to be sufficiently fast to agree with observed methane conversion rates.

The apparent overestimation of the reaction barriers and/or under-estimation of the Arrhenius pre-factor for the oxidation reactions could be caused by several factors. First, while we have searched several configurations for these reactions at the step edge and have reported the lowest-energy transition state configuration, it is possible that there is another, lower-energy transition state configuration that we did not find. Similarly, it is possible that a surface feature not investigated here, such as a kink, presents a more facile route for oxidation (and sufficiently fast to overcome the site's likely low surface population). In addition, it is possible that a contribution to the under-prediction of the rates for these reactions is error in the DFT calculations for this reaction class. The error in predicting the binding energy for O^* is found to be larger than for other species such as H^* ; however, the binding energy for CO^* is reasonably well-predicted by the DFT calculations carried out in this study. For example, if the C–O transition state energy is well-predicted by DFT like the CO^* binding energy, the error in treating the O^* binding energy could lead to over-prediction of the $C^* + O^* \rightarrow CO^*$ reaction barrier because, as shown in Tables 1 and 2, the experimentally-adjusted heats of adsorption treatment leads to a destabilization of O^* on Ni(211) by over 30 kJ/mol. However, the reaction barrier is not currently adjusted from the DFT-computed value because it is not known whether the transition state energy is well-predicted like CO^* , or predicted with error, like O^* .

The apparent under-prediction of the C–O addition reaction rates presents an area for further research. In

addition to the ability to more accurately predict SMR pathways, the carbon oxidation reactions represent an important branching point in understanding carbon formation (i.e., the competition between C–C coupling that leads to carbon formation and C–O coupling that oxidizes away carbon-containing intermediates). As we seek an improved understanding of the processes occurring on the catalyst surface, a physical description of this competition will be important in identifying the potential impact of new catalysts with regard to inhibition of carbon formation while retaining activity to the steam reforming reaction.

4 Conclusions

Density functional theory calculations are performed using the plane wave, periodic boundary condition Vienna Ab Initio Simulation Package to study the steam methane reforming reaction on a multi-faceted nickel catalyst, consisting of the Ni(111) surface, Ni(100) surface, and Ni step edges modeled using the Ni(211) surface. The introduction of additional facets to the microkinetic model describing SMR leads to a considerably improved description of overall methane conversion rates compared to our previously published Ni(111) reforming model. However, while the rate of dissociative methane adsorption is captured reasonably well by the present model, the rate(s) of carbon-containing intermediate species oxidation reaction(s) appear to be under-predicted because the model predicts that the oxidation reactions are rate-limiting in regions where it is believed, based on experiment, that dissociative methane adsorption is the rate-determining SMR step. For temperatures in excess of 800 °C, the model correctly predicts that dissociative methane chemisorption has the highest degree of rate control. Like previous results for the Ni(111) surface, the reaction of $CH^* + O^*$ to form CHO^* is predicted to be an important reaction on the Ni(211) surface, along with $C^* + OH^*$ to form COH^* on the Ni(211) and Ni(100) surfaces. However, at higher temperatures, the dominant reforming pathway is predicted to be through the direct formation of CO^* from C^* and O^* at the nickel step edge. The hydrogen-mediated pathways through intermediates such as COH^* and CHO^* are found to be active pathways in SMR at industrially-relevant temperatures, such as 800 °C; therefore, their inclusion in SMR kinetic models may be important. However, as a class of reactions, carbon-containing intermediate species oxidation rates appear to be under-predicted by the DFT methods applied in this study, suggesting further work is necessary to accurately capture these reactions. Describing these rates with reasonable accuracy is important for predicting the overall methane conversion rate in SMR as well as for understanding the competition between carbon

oxidation and carbon–carbon coupling, which can lead to coking and catalyst deactivation.

The present work does not include lateral adsorbate–adsorbate interactions, except for the correction of C* and CH* binding energies for C*–C* and CH*–CH* interactions as a function of surface coverage up to 0.5 ML. Because surface coverage of species, particularly on the Ni(100) surface and to some extent on the Ni(211) surface, is significant, it is possible that adsorbate–adsorbate interactions may play an appreciable role in surface thermochemistry and/or kinetics. These effects are ignored in the present study; however, an extension of the work to include these effects could provide additional insight into the system, though at a significant computational expense for a mechanism of this magnitude. It has been shown that a mean-field model with lateral interactions can capture interesting physics of systems without the need for more expensive kinetic Monte Carlo calculations, though this is a function of surface coverage and surface heterogeneity [46].

Acknowledgments The authors acknowledge the catalysis researchers at the Norwegian University of Science and Technology (NTNU), in particular Professors Anders Holmen and De Chen, for many helpful conversations. This work is funded, in part, through a collaboration with NTNU supported by StatoilHydro and the Norwegian Research Council. The National Science Foundation is also acknowledged for supporting D.W.B. through the Graduate Research Fellowship Program. In addition, the Norwegian Research Council and the National Science Foundation are acknowledged for support of D.W.B. through the Nordic Research Opportunity. This publication is also based on work supported, in part by King Abdullah University of Science and Technology (KAUST). The computations in this work have been supported in part by the National Science Foundation through TeraGrid resources provided by the NCSA, grant number TG-CHE080047. Finally, Yi-An Zhu acknowledges support by the Doctoral Fund of Ministry of Education of China (No. 200802511007).

References

- Solomon BD, Banerjee A (2006) A global survey of hydrogen energy research, development and policy. *Energy Policy* 34(7): 781–792
- US Department of Energy. Hydrogen Production Fact Sheet. 2006
- Lægsgaard Jørgensen S, Nielsen PEH, Lehrmann P (1995) Steam reforming of methane in a membrane reactor. *Catal Today* 25(3–4):303–307
- Chen Z, Yan Y, Elnashaie SSEHSEH (2004) Catalyst deactivation and engineering control for steam reforming of higher hydrocarbons in a novel membrane reformer. *Chem Eng Sci* 59(10):1965–1978
- Blok K, Williams RH, Katofsky RE, Hendriks CA (1997) Hydrogen production from natural gas, sequestration of recovered CO₂ in depleted gas wells and enhanced natural gas recovery. *Energy* 22(2–3):161–168
- Shishkin M, Ziegler T (2009) Oxidation of H₂, CH₄, and CO molecules at the interface between Nickel and Yttria-Stabilized Zirconia: a theoretical study based on DFT. *J Phys Chem C* 113(52):21667–21678
- Mogenssen D, Grunwaldt JD, Hendriksen PV, Dam-Johansen K, Nielsen JU (2010) Internal steam reforming in solid oxide fuel cells: status and opportunities of kinetic studies and their impact on modelling. *J Power Sources* 196(1):25–38
- Ingram DB, Linic S (2009) First-principles analysis of the activity of transition and noble metals in the direct utilization of hydrocarbon fuels at solid oxide fuel cell operating conditions. *J Electrochem Soc* 156(12):B1457–B1465
- Nørskov JK, Christensen CH (2006) Toward efficient hydrogen production at surfaces. *Science* 312(5778):1322–1323
- Sehested J (2006) Four challenges for nickel steam-reforming catalysts. *Catal Today* 111(1–2):103–110
- Pedernera MN, Piña J, Borio DO (2007) Kinetic evaluation of carbon formation in a membrane reactor for methane reforming. *Chem Eng J* 134(1–3):138–144
- Wei J, Iglesia E (2004) Isotopic and kinetic assessment of the mechanism of reactions of CH₄ with CO₂ or H₂O to form synthesis gas and carbon on nickel catalysts. *J Catal* 224(2):370–383
- Xu J, Froment GF (1989) Methane steam reforming, methanation and water-gas shift: I. Intrinsic kinetics. *AIChE J* 35(1):88–96
- Aparicio LM (1997) Transient isotopic studies and microkinetic modeling of methane reforming over nickel catalysts. *J Catal* 165(2):262–274
- Chen D, Lødeng R, Anundskås A, Olsvik O, Holmen A (2001) Deactivation during carbon dioxide reforming of methane over Ni catalyst: microkinetic analysis. *Chem Eng Sci* 56(4):1371–1379
- Dumesic JA, Rudd DF, Aparicio LM, Rekoske JE (1993) The microkinetics of heterogeneous catalysis. ACS Professional Reference Book, American Chemical Society, Washington, DC, p 315
- Chen D, Lødeng R, Svendsen H, Holmen A (2010) Hierarchical multiscale modeling of methane steam reforming reactions. *Industrial & Engineering Chemistry Research* (in Print)
- Jones G, Jakobsen JG, Shim SS, Kleis J, Andersson MP, Rossmel J, Abild-Pedersen F, Bligaard T, Helveg S, Hinnemann B, Rostrup-Nielsen JR, Chorkendorff I, Sehested J, Nørskov JK (2008) First principles calculations and experimental insight into methane steam reforming over transition metal catalysts. *J Catal* 259(1):147–160
- Zhu Y-A, Chen D, Zhou X-G, Yuan W-K (2009) DFT studies of dry reforming of methane on Ni catalyst. *Catal Today* 148(3–4): 260–267
- Nikolla E, Schwank J, Linic S (2009) Comparative study of the kinetics of methane steam reforming on supported Ni and Sn/Ni alloy catalysts: the impact of the formation of Ni alloy on chemistry. *J Catal* 263(2):220–227
- Bengard HS, Nørskov JK, Sehested J, Clausen BS, Nielsen LP, Molenbroek AM, Rostrup-Nielsen JR (2002) Steam reforming and graphite formation on Ni catalysts. *J Catal* 209(2):365–384
- Wang S-G, Cao D-B, Li Y-W, Wang J, Jiao H (2006) CO₂ reforming of CH₄ on Ni(111): a density functional theory calculation. *J Phys Chem B* 110(20):9976–9983
- Blaylock DW, Ogura T, Green WH, Beran GJO (2009) Computational investigation of thermochemistry and kinetics of steam methane reforming on Ni(111) under realistic conditions. *J Phys Chem C* 113(12):4898–4908
- Kresse G, Hafner J (1993) Ab initio molecular dynamics of liquid metals. *Phys Rev B* 47(1):558–561
- Kresse G, Furthmüller J (1996) Efficiency of ab initio total energy calculations for metals and semiconductors using a plane-wave basis set. *Comput Mater Sci* 6(1):15–50
- Kresse G, Furthmüller J (1996) Efficient iterative schemes for ab initio total-energy calculations using a plane-wave basis set. *Phys Rev B* 54(16):11169–11186

27. Klink C, Olesen L, Besenbacher F, Stensgaard I, Laegsgaard E, Lang ND (1993) Interaction of C with Ni(100): Atom-resolved studies of the “clock” reconstruction. *Phys Rev Lett* 71(26):4350
28. Hammer B, Hansen LB, Nørskov JK (1999) Improved adsorption energetics within density-functional theory using revised Perdew-Burke-Ernzerhof functionals. *Phys Rev B* 59(11):7413
29. Hammer B, Nørskov JK (2000) Theoretical surface science and catalysis—calculations and concepts. In: Hammer B, Nørskov JK (eds) *Advances in catalysis*, vol 45. Academic Press, New York, pp 71–129
30. Blöchl PE (1994) Projector augmented-wave method. *Phys Rev B* 50(24):17953
31. Henkelman G, Jonsson H (1999) A dimer method for finding saddle points on high dimensional potential surfaces using only first derivatives. *J Chem Phys* 111(15):7010–7022
32. Henkelman G, Uberuaga BP, Jonsson H (2000) A climbing image nudged elastic band method for finding saddle points and minimum energy paths. *J Chem Phys* 113(22):9901–9904
33. Henkelman G. <http://theory.cm.utexas.edu/vtsttools/dynmat/>. Accessed Nov 2010
34. Li H, Zhao M, Jiang Q (2009) Cohesive energy of clusters referenced by Wulff construction. *J Phys Chem C* 113(18):7594–7597
35. Greeley J, Rossmeisl J, Hellmann A, Nørskov JK (2007) Theoretical trends in particle size effects for the oxygen reduction reaction. *Z Phys Chem* 221(9–10):1209–1220
36. Honkala K, Hellman A, Remediakis IN, Logadottir A, Carlsson A, Dahl S, Christensen CH, Nørskov JK (2005) Ammonia synthesis from first-principles calculations. *Science* 307(5709):555–558
37. Jiang Q, Lu HM, Zhao M (2004) Modelling of surface energies of elemental crystals. *J Phys Condens Matter* 16(4):521–530
38. Cwiklik L (2007) Influence of surface diffusion on catalytic reactivity of spatially inhomogeneous surfaces—mean-field modeling. *Chem Phys Lett* 449(4–6):304–308
39. Lapujoulade J, Neil KS (1972) Chemisorption of hydrogen on the (111) plane of nickel. *J Chem Phys* 57(8):3535–3545
40. Lapujoulade J, Neil KS (1973) Hydrogen adsorption on Ni (100). *Surf Sci* 35:288–301
41. Stuckless JT, Al-Sarraf N, Wartnaby C, King DA (1993) Calorimetric heats of adsorption for CO on nickel single crystal surfaces. *J Chem Phys* 99(3):2202–2212
42. Stuckless JT, Wartnaby CE, Al-Sarraf N, Dixon-Warren SJB, Kovar M, King DA (1997) Oxygen chemisorption and oxide film growth on Ni{100}, {110}, and {111}: Sticking probabilities and microcalorimetric adsorption heats. *J Chem Phys* 106(5):2012–2030
43. Liu Z-P, Hu P (2003) General rules for predicting where a catalytic reaction should occur on metal surfaces: a density functional theory study of C-H and C-O bond breaking/making on flat, stepped, and kinked metal surfaces. *J Am Chem Soc* 125(7): 1958–1967
44. Jiang T, Mowbray DJ, Dobrin S, Falsig H, Hvolbæk B, Bligaard T, Nørskov JK (2009) Trends in CO oxidation rates for metal nanoparticles and close-packed, stepped, and kinked surfaces. *J Phys Chem C* 113(24):10548–10553
45. Jakobsen JG, Joergensen TL, Chorkendorff I, Sehested J (2010) Steam and CO₂ reforming of methane over a Ru/ZrO₂ catalyst. *Appl Catal A* 377(1–2):158–166
46. Dooling DJ, Broadbelt LJ (2001) Microkinetic models and dynamic Monte Carlo simulations of nonuniform catalytic systems. *AIChE J* 47(5):1193–1202